nature catalysis

Article

https://doi.org/10.1038/s41929-023-01003-5

Cationic-group-functionalized electrocatalysts enable stable acidic CO_2 electrolysis

Received: 25 July 2022

Accepted: 12 July 2023

Published online: 21 August 2023

Check for updates

Mengyang Fan[1,7], Jianan Erick Huang[2,7], Rui Kai Miao[1,7], Yu Mao[3,7], Pengfei Ou[2,4,7], Feng Li[1], Xiao-Yan Li[2], Yufei Cao[2], Zishuai Zhang[5], Jinqiang Zhang[1,2], Yu Yan[2], Adnan Ozden[1], Weiyan Ni[2], Ying Wang[6], Yong Zhao[1], Zhu Chen[2], Behrooz Khatir[1], Colin P. O'Brien[1], Yi Xu[1], Yurou Celine Xiao[1], Geoffrey I. N. Waterhouse[3], Kevin Golovin[1], Ziyun Wang[3] ✉, Edward H. Sargent[2,4] ✉ & David Sinton[1] ✉

Acidic electrochemical CO_2 reduction (CO_2R) addresses CO_2 loss and thus mitigates the energy penalties associated with CO_2 recovery; however, acidic CO_2R suffers low selectivity. One promising remedy—using a high concentration of alkali cations—steers CO_2R towards multi-carbon (C_{2+}) products, but these same alkali cations result in salt formation, limiting operating stability to <15 h. Here we present a copper catalyst functionalized with cationic groups (CG) that enables efficient CO_2 activation in a stable manner. By replacing alkali cations with immobilized benzimidazolium CG within ionomer coatings, we achieve over 150 h of stable CO_2R in acid. We find the water-management property of CG minimizes proton migration that enables operation at a modest voltage of 3.3 V with mildly alkaline local pH, leading to more energy-efficient CO_2R with a C_{2+} Faradaic efficiency of 80 ± 3%. As a result, we report an energy efficiency of 28% for acidic CO_2R towards C_{2+} products and a single-pass CO_2 conversion efficiency exceeding 70%.

Electrochemical CO_2 reduction (CO_2R) offers a route to produce fuels and chemicals with low carbon intensity[1–3]. CO_2R towards multi-carbon (C_{2+}) products has reached Faradaic efficiencies (FEs) of 70–80% at relevant current densities (>100 mA cm^{-2}) in CO_2R-favourable alkaline and neutral reaction environments[4–7]. However, at these conditions, the loss of reactant CO_2 to carbonate species limits the single-pass CO_2 conversion efficiency (SPC) (<5%) and thus leads to a significant extra energy cost to regenerate CO_2 from electrolyte[8–11].

Acidic electrolytes eliminate carbonate formation, enabling high SPC (70–80%) (refs. 12–14); but CO_2R kinetics are outcompeted by hydrogen evolution reaction (HER) at low pH[13,15,16]. Adding a high concentration of alkali cations to the electrolyte can help steer the reaction to CO_2R. However, alkali cations essential for CO_2R in acidic conditions accumulate, leading to the crystallization of alkali salts on the catalyst and gas diffusion electrode that limit the lifetime of the cell[17,18]. Pulsed electrolysis with a range of duty cycles enables the mitigation of salt formation[17]; however, the CO_2R performance is compromised by HER due to the local pH change after the open circuit potential (OCP) cycles in acidic conditions. Thus, acidic CO_2R suffers a trade-off between C_{2+} selectivity and stability.

[1]Department of Mechanical and Industrial Engineering, University of Toronto, Toronto, Ontario, Canada. [2]Department of Electrical and Computer Engineering, University of Toronto, Toronto, Ontario, Canada. [3]School of Chemical Sciences, The University of Auckland, Auckland, New Zealand. [4]Department of Chemistry, Northwestern University, Evanston, IL, USA. [5]Department of Chemistry, The University of British Columbia, Vancouver, British Columbia, Canada. [6]Department of Chemistry, The Chinese University of Hong Kong S. A. R., Ma Liu Shui, China. [7]These authors contributed equally: Mengyang Fan, Jianan Erick Huang, Rui Kai Miao, Yu Mao, Pengfei Ou. ✉e-mail: ziyun.wang@auckland.ac.nz; ted.sargent@utoronto.ca; sinton@mie.utoronto.ca

https://doi.org/10.1038/s41929-023-01003-5

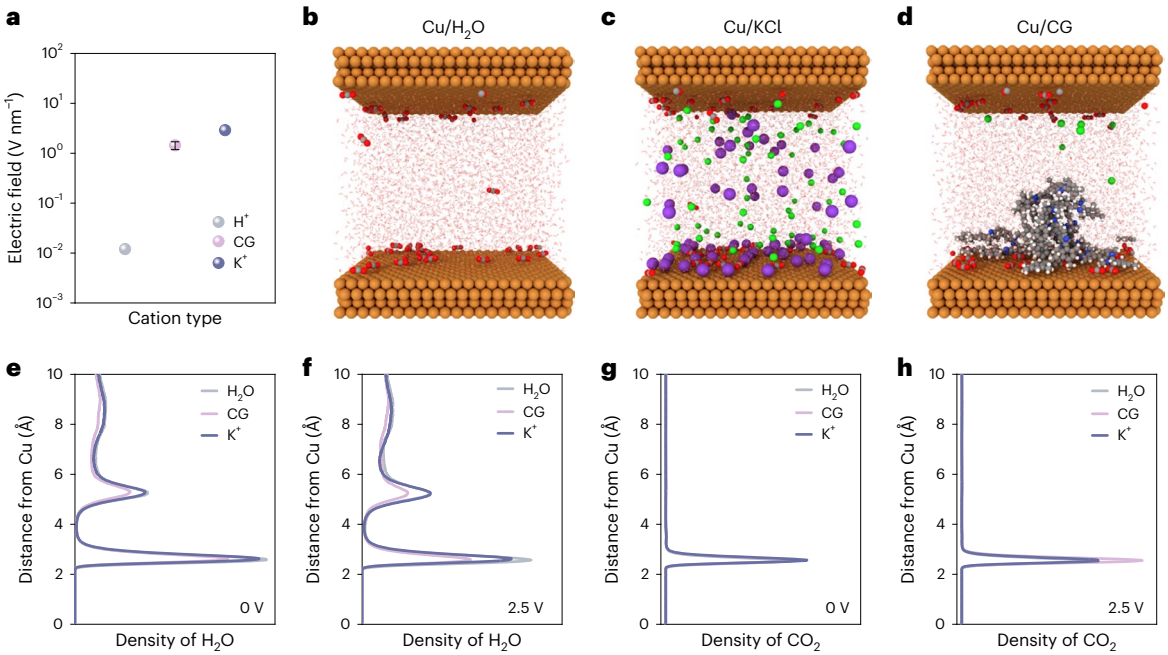

Fig. 1 | Computational studies of CG-functionalized catalysts in acidic CO_2R. **a**, Electric field comparison of H^+, K^+ and immobilized CG at OHP. The electric field value of CG is average, and the error bar indicates the maximum and minimum electric field values calculated according to the estimated hydrated radius shown in Supplementary Note 2. **b**–**d**, MD model predictions of atomic configurations for the Cu/H_2O (**b**), Cu/KCl (**c**) and Cu/CG (**d**) systems at the end of NVE simulation (ΔU = 2.5 V). Red, grey, yellow, green, purple, blue and white balls represent O, C, Cu, Cl, K, N and H, respectively. **e**,**f**, Comparison of simulated density of H_2O versus distance from the Cu electrode at fixed potential (ΔU) of 0 V (**e**) and 2.5 V (**f**). **g**,**h**, Comparison of simulated density of CO_2 versus distance from the Cu electrode at fixed potential (ΔU) of 0 V (**g**) and 2.5 V (**h**). Atomic configurations at the start of NVE simulation (ΔU = 0 V) are shown in Supplementary Fig. 9. ΔU, potential difference between two electrodes.

In this Article, we pursued an immobilized cationic group (CG) decorated strategy to improve both the C_{2+} selectivity and stability in a strongly acidic environment (0.2 M H_2SO_4, pH 0.4). We integrate a thin layer of ionomer with immobilized cationic functional groups at the Cu surface in place of the electrolyte alkali cation. This layer also lowers the proton diffusion rate and increases the local pH for selective C_{2+} products. In contrast to the previous acidic work, where a high current density (-1 A cm^{-2}) is necessary to overcome HER, we can operate productively at a moderate current density (-100 mA cm^{-2}) and thus avoid excessive voltage losses due to cell resistance. When operated at 100 mA cm^{-2}, the system maintains 90% SPC of CO_2 and requires a full-cell voltage of 3.3 V. By applying an extra carbon-Nafion layer for uniform ionic current distribution and protection from the direct proton flux, we achieve stable operation (>150 h) and total C_{2+} FE of 80%. The strategy presented here provides a catalyst design principle for stable, energy- and carbon-efficient CO_2R.

Results

Alkali cation versus cationic functional group in acidic media

Alkali cations facilitate CO_2R in strongly acidic environments by modifying the interfacial electric field and buffering local pH[15,19,20] (Supplementary Note 1 and Supplementary Figs. 1 and 2). The high concentration of alkali cations accumulates at cathode surface, leading to salt formation issue (Supplementary Fig. 3 and Supplementary Table 1). We have operated pulsed electrolysis to mitigate the salt issue; however, the CO_2R selectivity decreases with an increasing HER after OCPs (Supplementary Fig. 4a)—an effect we attribute to reduced alkalinity during the OCP step. The catalyst surface was destroyed by the strong acid when no current or potential was applied during the OCP cycles (Supplementary Fig. 4b).

In addition to the extensive studies on the role of alkali cations in promoting CO_2R (refs. 13,15,16,21), prior work has suggested that immobilized CG in ionic liquids or surfactants—including ammonium CG[22], imidazolium CG[23] and benzimidazole CG[24]—can also stabilize key intermediates and promote CO_2R to multi-carbon products. These same CG can also bind with functional backbones[25] that potentially influence H_3O^+ transport.

We predicted the interfacial electric field of the immobilized CG (benzimidazole CG) and the alkali cation (K^+) using the modified Poisson–Boltzmann model in COMSOL. We found the interfacial electric field generated by CG was of the same order of magnitude as that generated by K^+ (Fig. 1a, Supplementary Note 2 and Supplementary Figs. 5 and 6). The surface electric field generated by cations has a stabilization effect on the negatively charged CO_2 and facilitates CO_2 adsorption and activation in acidic media (Supplementary Fig. 7)[13,15]. In contrast, we found the effect of H^+ on the electric field to be negligible compared with that of both the CG or K^+ ions. We examined the water-management effect via molecular dynamics (MD), quantifying the distribution of H_2O and CO_2 near the Cu surface. The surface modified with the CG showed the lowest density of H_2O compared with K^+ and pure water cases at different potentials (Fig. 1b–f, Supplementary Note 3 and Supplementary Figs. 8–15), indicating H_3O^+-blocking function. Additionally, the CG layer enhanced the local CO_2 concentration at the Cu surface when a constant potential was applied (Fig. 1b–d,g,h, Supplementary Fig. 15 and Supplementary Videos 1–3)[26].

Inspired by the cation effect and H_3O^+ tuning effect predicted by the computational results, we pursued a immobilized cation enrichment strategy deploying a layer of ionomer with the cationic functional groups, one that could vary the concentration of positive benzimidazolium CG on the Cu catalyst (Methods)[27–29]. The number of the CG per dry ionomer is indicated by its ion exchange capacity (IEC). We began with a low concentration of CG (CG-low) that has the lowest water uptake, with which we expected to maximize the local pH and minimize proton migration to the Cu surface.

https://doi.org/10.1038/s41929-023-01003-5

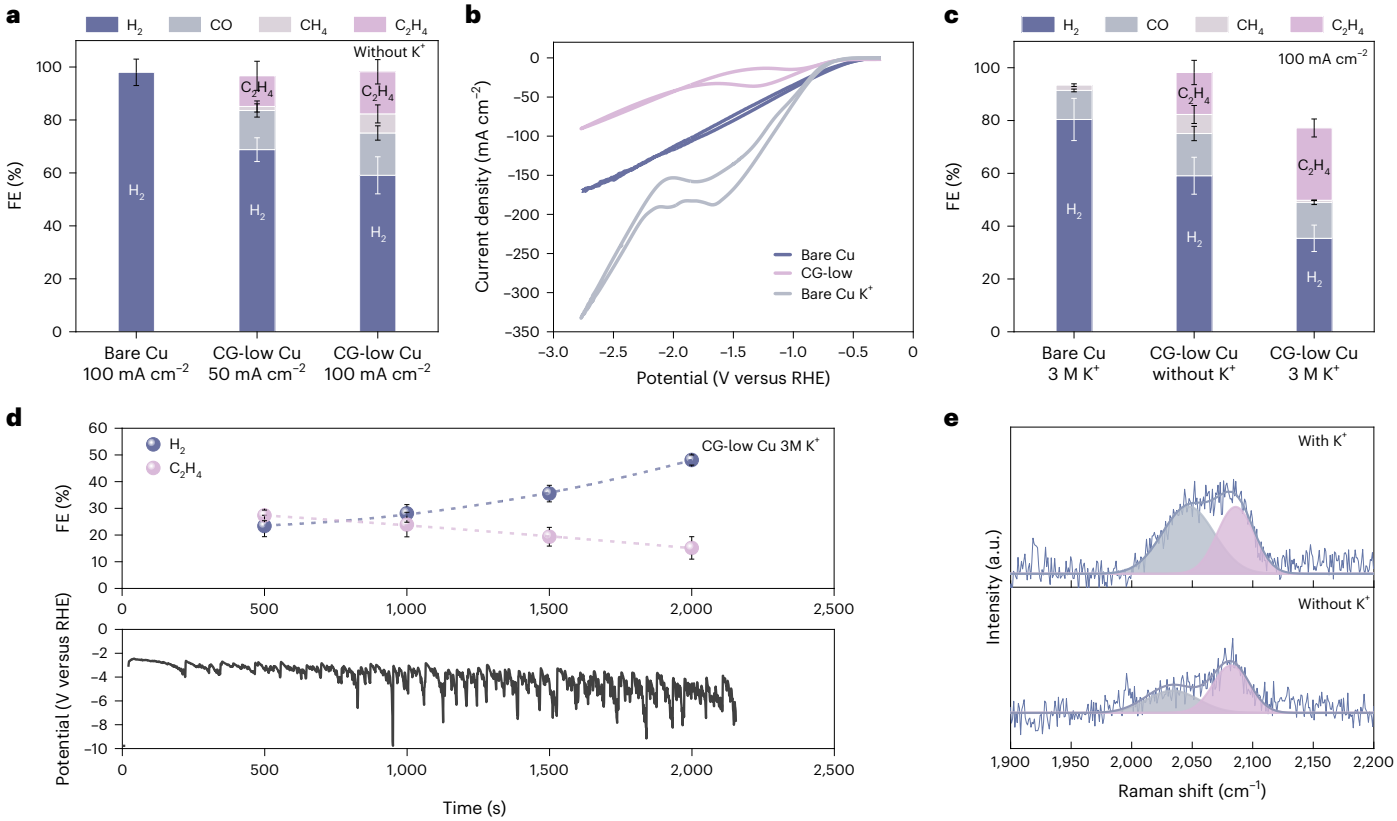

Fig. 2 | Cationic functional group enables CO_2R in acidic media. a, Selectivity of bare Cu at a current density of 100 mA cm^{-2} and CG-low Cu at current densities of 50 and 100 mA cm^{-2}. Values are means, and error bars indicate s.d. ($n = 3$ replicates). **b**, CV curves of bare Cu (purple), CG-low Cu (pink) in 0.2 M H_2SO_4 with Ar and bare Cu (grey) in 0.2 M H_2SO_4 + 3 M KCl with Ar. Scan rate was 100 mV s^{-1}. **c**, Selectivity of bare Cu and CG-low Cu in 0.2 M H_2SO_4 solution with and without K^+ at a current density of 100 mA cm^{-2}. Values are means, and error bars indicate s.d. ($n = 3$ replicates). **d**, FE (top) and potential degradation (bottom) of CG-low Cu at a constant current density of 100 mA cm^{-2}. As the catholyte, 0.2 M H_2SO_4 with 3 M K^+ was used during 30 min. Formation of H_2 bubbles affected the reference electrode and gradually increased noise in the collected potential signals. Values are means, and error bars indicate s.d. ($n = 3$ replicates). **e**, In situ surface-enhanced Raman spectra of CO_{atop} on CG-low Cu. The results were obtained at a constant potential −1.34 V versus RHE. The atop-bound CO was deconvolved into two peaks at HFB (pink) and LFB (grey).

We first examined the CO_2R performance of CG-low Cu catalyst in a flow cell with a gas diffusion electrode, employing 0.2 M H_2SO_4 as both catholyte and anolyte. Varying the CG-low loading did not show significant impact on the performance when there was full coverage of the immobilized CG layer (Supplementary Fig. 16). The CG-low Cu showed a reduced H_2 FE of 60%, and CO_2R products were observed at current densities of 50 and 100 mA cm^{-2} (Fig. 2a—an improvement over the negligible amount of CO_2R (<1%) observed on the bare Cu case at similar electrolyte bulk pH with K^+. To elucidate the reason of this improvement, we carried out cyclic voltammetry (CV) of CG-low Cu and bare Cu in H_2SO_4 electrolytes, with and without K^+. The onset of the plateau that represents the depletion of H_3O^+ at the Cu surface is at a lower current with CG-low Cu compared with bare Cu in K^+ rich electrolyte (Fig. 2b), indicating a proton barrier effect and higher local pH in the CG-low case, consistent with the prediction of MD simulation results. We then evaluated the electric field and compared it between K^+ and CG-low by performing potential-dependent in situ surface-enhanced Raman spectroscopy (SERS) and calculating the Stark tuning rate[30] (Supplementary Note 4). On CG-low modified Cu, we observed the CO adsorption occupying both terrace and low coordination sites of Cu, similar to that of pure K^+, but the slightly lower stark tuning rate indicates a smaller surface electric field strength (Supplementary Fig. 17). We posited that CO_2R activity could be further enhanced with a higher population of CG, as the enhanced electric field can stabilize negatively charged CO_2 intermediates[15,21,31].

To test this hypothesis, we carried out control studies to examine the performance of CG-low Cu in H_2SO_4 with the addition of KCl. We detected increased CO_2R FE, especially towards C_{2+} products such as C_2H_4 (FE 27 ± 2%) at 100 mA cm^{-2} with 3 M KCl (Fig. 2c and Supplementary Figs. 18 and 19). This result indicated that the presence of alkali cation accelerates the CO_2R kinetics on the CG-low Cu surface. The effect of anion species on CO_2R selectivity was not significant (Supplementary Fig. 20). However, the excess of local OH^- and K^+ ions led to salt formation at the catalyst and gas channel layers, and a rapid decay in C_2H_4 FE from 27% to 15% with an increase in H_2 FE from 20% to 48% (Fig. 2d).

To explain the initially lower HER and improvement in C_{2+} FE, we measured the CV and in situ SERS in the electrolytes, with and without K^+ on CG-low Cu. With the additional cations, the onset of the current plateau of H_3O^+ depletion takes place at slightly lower current and overpotential (Supplementary Fig. 21). The additional cation thus further confines the electrical double layer (EDL) and decreases the rate of H_3O^+ migration towards the outer Helmholtz plane (OHP)[25]. In the absence of the K^+, the benzimidazolium group is the only cation near the electrode–electrolyte interface. The in situ SERS spectrum showed increasing peak intensities from 1,000 cm^{-1} to 1,100 cm^{-1}, the frequencies that are associated with the breathing vibration of benzene rings in the benzimidazolium unit, as we ramped up the reductive potential at cathode (Supplementary Fig. 22a). This suggested that the CG (positively charged nitrogen) near the electrode are oriented closer to the negatively charged Cu surface under the increasing

https://doi.org/10.1038/s41929-023-01003-5

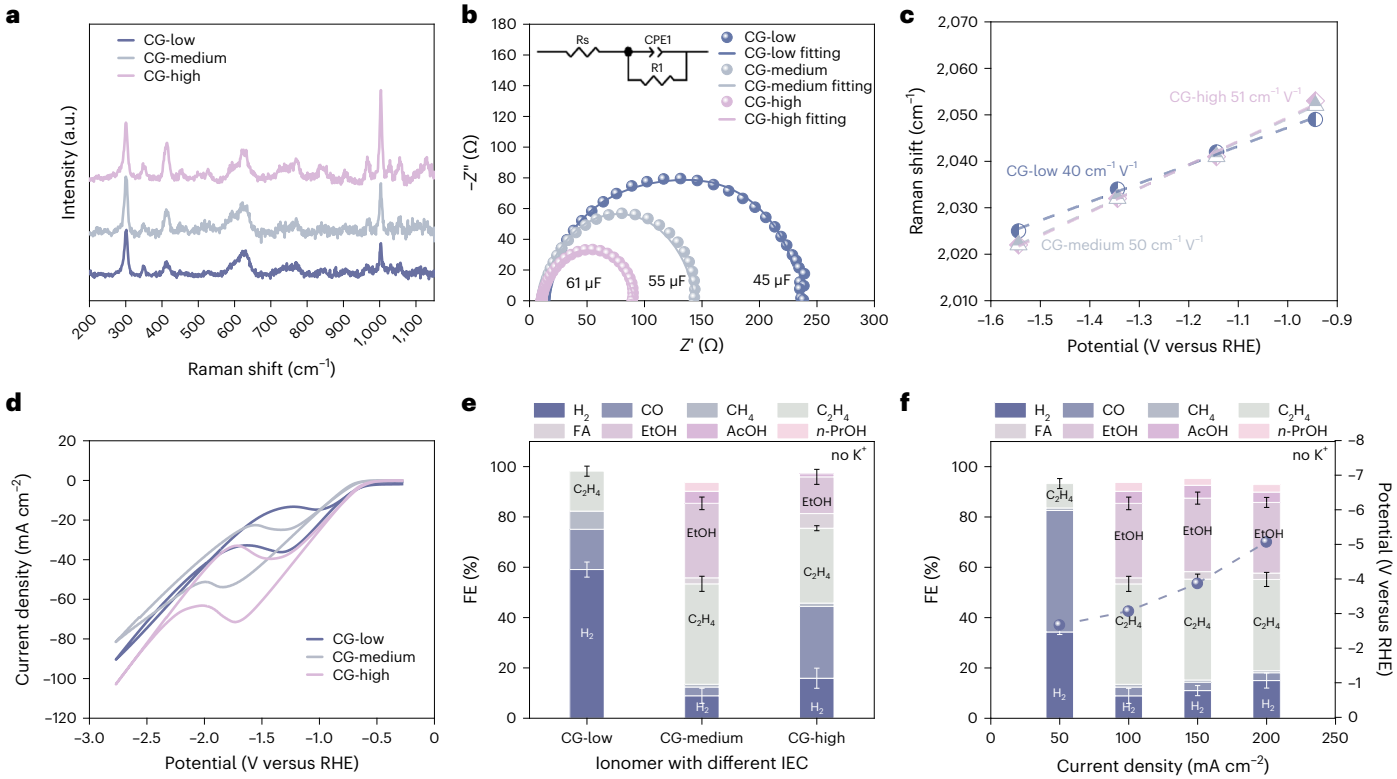

Fig. 3 | Performance of the CG-functionalized catalysts in acid media. a, Ex situ Raman spectroscopy of CG-low (purple), CG-medium (grey) and CG-high (pink). The characteristic vibration of benzyl group is from 900 cm^{-1} to 1,100 cm^{-1}. The peak intensity is normalized by characteristic peak of Cu–O at 300 cm^{-1}. **b**, EIS measurements for effective EDL capacitance of CG-low, CG-medium and CG-high in 0.2 M H_2SO_4. The EIS data were obtained between 0.1 Hz and 10 kHz. The effective double-layer capacitance (C_{dl}) was obtained from the constant phase element (CPE) parameters and the two resistances using the Brug formula. Inset: equivalent circuit for EIS fitting. **c**, Stark tuning slope comparison of CG-low, CG-medium and CG-high. The atop-bound CO_{ads} vibration frequencies in Supplementary Fig. 25 were used to calculate the Stark tuning slope in **c**. **d**, CV curves of bare CG-low, CG-medium and CG-high in 0.2 M H_2SO_4 with Ar. Scan rate was 100 mV s^{-1}. **e**, Selectivity comparison of CG-low, CG-medium and CG-high in 0.2 M H_2SO_4 solution at a current density of 100 mA cm^{-2}. Values are means, and error bars indicate s.d. ($n = 3$ replicates). **f**, Selectivity comparison of CG-medium Cu at different operating current densities. The tests were carried out in 0.2 M H_2SO_4 with a CO_2 flow rate of 50 sccm. Values are means, and error bars indicate s.d. ($n = 3$ replicates). FA, formic acid.

Table 1 | Metrics of ionomers with benzimidazolium cationic functional groups

Type	IEC[a] (mEq g^{-1})	Conductivity (mS cm^{-1})	Water uptake[b] (%)
CG-low	0.5–0.6	1.3–2.5	13–15
CG-medium	1.4–1.7	2–4	35–50
CG-high	2.3–2.6	8–11	95–100

[a]IEC in the hydroxide (OH^-) counter-ion form. [b]Approximate swelling properties when cast into membrane form at 25–50 μm.

electrostatic interactions[32,33]. With the addition of KCl in the electrolyte, we observed an obvious decrease in the peak intensity, indicating a compact cation layer with the binding of hydrated K^+ that replaced the benzimidazolium group near the Cu surface (Supplementary Fig. 22b). To evaluate the OHP generated by the cation layer, which is correlated with the electric field strength, we quantified the EDL values of CG-low with and without K^+ addition and compared them with the bare Cu with K^+ case (Supplementary Fig. 23, Supplementary Note 5 and Supplementary Table 2). The EDL of CG-low without K^+ addition is smaller than the bare Cu with 3 M K^+, in agreement with the trend of Stark tuning slope measured by in situ SERS. Adding K^+ to the CG-low Cu increases the EDL, indicating a larger OHP that potentially enhances the intermediate adsorption on catalyst surface through enhanced surface electric interactions. Potential-dependent SERS was carried out on CG-low modified Cu in 3 M K^+ electrolyte, and the Stark tuning slope was higher than that induced by mere CG-low. This indicates a stronger interfacial electric field near Cu surface in the K^+ enriched case, consistent with the EDL results (Supplementary Fig. 24). We then compared in situ SERS spectra of Cu-CO in both electrolytes (with and without K^+) to qualitatively assess the cation layer effect on CO adsorption, the main intermediate in CO_2R. When the K^+ was added into the electrolyte on CG-low modified Cu, at the same electrode potential, we observed a substantial increase in both high-frequency band (HFB) and low-frequency band (LFB) peak area (Fig. 2e), indicating more adsorbed CO on both terrace and low coordination Cu sites and thus fewer sites for H_2 formation. We also found that, in the presence of K^+, the CO occupancy on the terrace site increased more than that on low coordination site (Supplementary Table 3). The improvement in the C_{2+} selectivity is thus attributed to the enhanced surface electric field that significantly increase the CO population, especially on the terrace sites that favour the C–C coupling reaction, albeit at the cost of salt formation and catalyst degradation[21,34,35].

Tuning the CG layer in non-alkali electrolyte

To further improve the FE towards C_{2+} products without relying additional alkali cations in solution, we increased the CG concentration. We evaluated the performance of higher CG concentration loaded samples, CG-medium and CG-high modified Cu, at the same condition (pure 0.2 M H_2SO_4). The increased CG population was confirmed via IEC (Table 1)[36]. The higher CG concentrations were further confirmed through SERS and surface capacitance. The normalized solid-state

https://doi.org/10.1038/s41929-023-01003-5

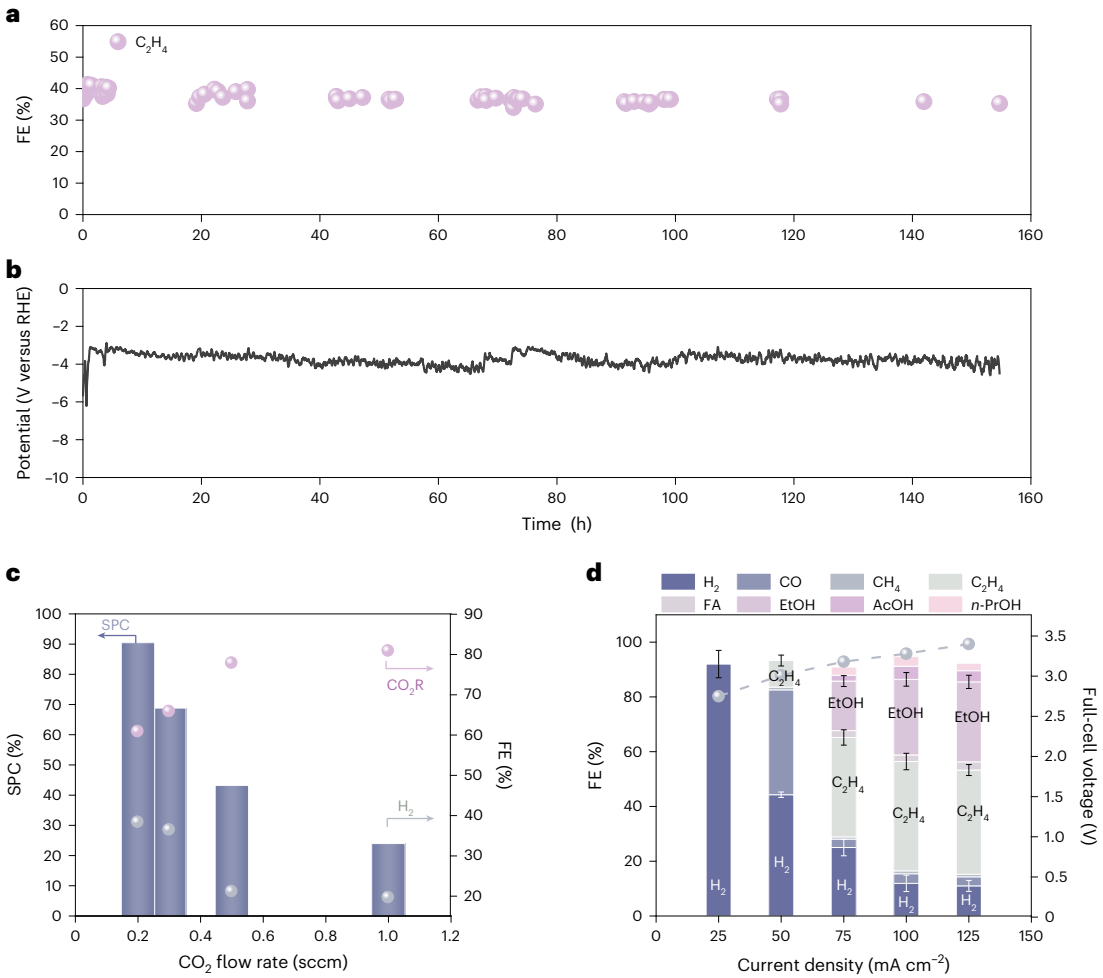

Fig. 4 | Stability and SPC performance of carbon-protected CG-medium Cu in acidic media. a,**b**, FE towards C_2H_4 (**a**) and recorded potential (**b**) at constant current density of 100 mA cm^{-2} during 155 h of continuous CO_2R. **c**, SPC of CO_2 at various flow rates. **d**, Full-cell-voltage performance in a slim flow cell at applied current densities from 25 mA cm^{-2} to 125 mA cm^{-2}. Values are means, and error bars indicate s.d. ($n = 3$ replicates). The tests were carried out in the electrolyte of 0.2 M H_2SO_4.

spectrum of the CG-medium and CG-high showed higher peak intensity from 1,000 cm^{-1} to 1,100 cm^{-1}, the frequencies that are associated with the breathing vibration of benzene rings in the benzimidazolium unit (Fig. 3a)[37–39]. There is an observed increase of EDL for CG-medium and CG-high, indicating an enhanced electric field trend when increasing the CG concentration. (Fig. 3b and Supplementary Table 4). Increasing CG concentration (that is, CG-medium and CG-high modified Cu), the CO coverage increased on the basis of the integrated area of ν(CO) (Supplementary Fig. 25), which we take as a result of both the increasing amount of available CO_2 molecule near the surface (Supplementary Fig. 15) and faster rate of CO_2 activation due to the increased surface charge density and electric field (Fig. 3c and Supplementary Fig. 25)[13,15].

Despite the merits of a high CG concentration and high ionic conductivity, high IEC will also lead to enhanced water uptake of the CG layer and greater proton access[40] (Table 1 and Supplementary Fig. 26). In acidic electrolyte, this results in rapid proton influx and a lower local pH unfavourable for CO_2R. To test this hypothesis, we first measured the CV curve of three different concentration CG samples (CG-low, CG-medium and CG-high) in pure H_2SO_4 electrolyte (0.2 M) to investigate the proton depletion current. As expected, the plateau current of HER increased with the increasing IEC and water uptake, indicating a faster H_3O^+ migration from the bulk electrolyte when a higher CG concentration layer is applied (Fig. 3d). Although a higher CG concentration is desired at OHP, the enhanced water uptake compromises the effectiveness of the CG layer as proton barrier[41,42]. It is therefore important to tune both the CG density and water/proton permeability to reach the highest C_{2+} FE.

We then tested the performance of CG-modified Cu at a range of acid concentrations (Supplementary Fig. 27). The best result sustained over a 1 h test was that of CG-medium Cu, with an FE of 40 ± 2% towards C_2H_4, much lower HER (<10%) and a total C_{2+} FE of 80 ± 3% at current density of 100 mA cm^{-2} (Fig. 3e,f and Supplementary Fig. 28). CG-high resulted in more CO detected (28 ± 2%) and less total C_{2+} products to 60 ± 4%. The slightly higher CO FE and less C_2H_4 FE on CG-high modified Cu, which is also consistent with the lower CO_{ads} terrace ratio observed from in situ SERS (Supplementary Fig. 25 and Supplementary Table 5), was attributed to the higher water uptake that increases the proton transfer from bulk to the Cu surface and thus lowers the local pH (Fig. 3d). To quantify its value and directly compare the local pH of CG-medium and CG-high, we used 0.5 M H_3PO_4 solution as a pH indicator during in situ SERS measurement. We recorded the signal areas of H_3PO_4, $H_2PO_4^-$, HPO_4^{2-} and PO_4^{3-} and used the equilibrium of $H_3PO_4/H_2PO_4^-/HPO_4^{2-}/PO_4^{3-}$ to calculate the local pH (Supplementary Note 6 and Supplementary Table 6). At 150 mA cm^{-2} operating current density, the local pH of CG-high Cu is calculated to be ~12.6, slightly lower than that of CG-medium Cu's ~12.9 (Supplementary

Fig. 29 and Supplementary Table 7). The lower local pH leads to a kinetic competition between CO desorption and C–C coupling that reduces C_{2+} selectivity (Supplementary Figs. 30 and 31)[43,44]. Adding more K^+ sources into the electrolyte enhanced the EDL structure of CG-medium and CG-high, but the local pH was affected by the increasing water permeability introduced by the hydrated K^+ (Supplementary Note 7, Supplementary Figs. 32–35 and Supplementary Table 8). Similar to the CG-low case, the additional K^+ containing electrolytes resulted in severe salt precipitation and rapid performance degradation (Supplementary Fig. 36)

In non-alkali acidic electrolyte, CG-medium creates a productive catalytic condition that balances cation group density and water uptake. Concentrated immobilized non-alkali CG enable stable CO_2R performance with H_2 FE less than 10% and C_{2+} FE around 80%. The benefit brought by further increasing CG concentration is limited and will be compromised by the higher water uptake that leads to faster H_3O^+ migration.

Acidic CO_2R performance with the CG-modified catalyst

Replacing the alkali metal cation in the solution with a layer of CG on Cu should reduce salt formation and thereby remove a leading cause of poor system stability. However, CG-medium Cu (in 0.2 M H_2SO_4) provided C_2H_4 FE >35% for less than 1 h (Supplementary Fig. 37). We observed dark spots formed on the Cu (Supplementary Fig. 38), which we attribute to the corrosion of Cu as the protective cation group layer decayed over time, followed by an uneven distribution of current density. The hydration of CG over the layer proceeds at different rates, leading to non-uniformities in hydration, ionic conductivity and access for protons to oxidize the Cu underneath. We applied a layer of carbon nanoparticles (CNPs) atop the CG layer to serve as a physical barrier to limit the proton transfer. The carbon layer may also provide the electrode some protection from electrolyte impurities detrimental to CO_2R performance and stability[45] (Supplementary Table 9). This layer was made up of CNPs bound with Nafion to prevent breakdown of the CG layer due to non-uniform hydration and ionic conductivity. This protective layer reduces the proton flux through the CG layer by enhancing the surface hydrophobicity and does not substantially change its EDL structure (Supplementary Figs. 39 and 40 and Supplementary Table 10). The Nafion/carbon-protected CG-medium Cu operated for over 150 h in strong acid, with a steady C_2H_4 FE of over 40% (Fig. 4a,b). The carbon-protected CG layer remained intact after >150 h operation (Supplementary Fig. 41). Only trace K^+ was detected in the electrolyte after 80 h of electrolysis (Supplementary Table 11).

The lack of salt formation in this system also benefits CO_2 utilization. CO_2 is regenerated within the bulk electrolyte and fed back to the gas inlet. We pursued a high SPC to reduce further the product separation costs. SPC is calculated using the fraction of the input CO_2 supply that is converted to CO_2R products. By throttling the input CO_2, we achieved 90% SPC for all CO_2R products (Fig. 4c). Further employing a slim flow cell with low resistance (Supplementary Fig. 42), we operated the carbon-coated CG-medium Cu at current densities from 50 to 150 mA cm^{-2}, and the full-cell voltage at 100 mA cm^{-2} was 3.3 V (without iR compensation) with a C_{2+} FE of 80%, leading to a record C_{2+} energy efficiency (EE) of 28% for acid CO_2R system (Fig. 4d). We assessed pure water electrolysis in a zero-gap system using Nafion as the proton conductor. The FE towards C_2H_4 was similar to that in acidic electrolyte, but the high ionic resistance of pure water led to high full-cell voltage and low EE (Supplementary Fig. 43).

Conclusions

This work demonstrates that CO_2R in an acidic environment can be achieved without alkali metal cations in solution and the associated challenges of salt formation and CO_2 loss. Immobilized cationic functional groups generate a surface electric field and provide a buffer of local acidity that enables CO_2 activation and C–C coupling in the presence of strong acid. We demonstrate that the local environment can be made productive for C_{2+} without requiring high current densities that incur severe energy costs. Operating at a moderate current density of 100 mA cm^{-2}, we achieve 80% C_{2+} FE and 9% H_2 FE in a strong acid environment (pH 0.4) with no alkali metal cations in solution. This approach requires a full-cell potential of 3.3 V (iR-free) to operate CO_2R at an industrially relevant reaction rate of 100 mA cm^{-2}. By avoiding carbonate salt formation from alkali metal ions, the stability of this acidic system exceeds 150 h. Additionally, loss of CO_2 is minimized, and the maximum SPC exceeds 90%. This study highlights a strategy to design CO_2R catalysts in non-alkali acidic electrolytes that eliminates the energy cost related to salt formation and enables prolonged CO_2R in acidic conditions.

Methods

Preparation of Cu electrodes

The Cu electrode was prepared by sputtering pure Cu (>99.99%, Kurt J. Lesker) onto a polytetrafluoroethylene gas diffusion layer with 450 nm pore size. The sputtering was carried out in an Angstrom Nexdep sputtering system in a vacuum environment (~10^{-5}–10^{-6} torr) with a deposition rate of 1 Å s^{-1}. The thickness of the sputtered Cu layer was 200 nm.

Preparation of CG-modified Cu electrodes

The CG-modified Cu electrodes were fabricated by spraying 1 wt% ionomer solutions with different cationic functional group densities and the spray loadings were kept constant at 3 mg cm^{-2}.

All three CG-low, CG-medium and CG-high ionomers were prepared by dissolving three types of ionomer dry resin (Aemion$^+$, ionomer AP2-HNN2-00, AP2-HNN5-00 and AP2-HNN8-00, respectively) in a solvent composed of 80/20 vol.% ethanol (>99.5%, Sigma-Aldrich)/acetone (>99.5%, Fisher Chemical) to yield a 1 wt% ionomer solution. The spray loading of the ionomer solution was adjusted from 1 to 3 mg cm^{-2}. Carbon-protected CG-Cu was prepared by spray coating CNP ink onto the CG-modified Cu. The CNP ink was composed of 4 mg CNP (Vulcan XC 72R) and 0.035 g Nafion solution (5 wt%, D520 Dispersion) dispersed in 15 ml methanol (>99.8%, Fisher Chemical). The CNP ink was sonicated for at least 1 h before spray coating.

Electrochemical reduction of CO_2

The CO_2R was carried out in a three-electrode flow cell, where CG-modified Cu as the cathode electrode with an exposed size of 1 cm^2, an Ag/AgCl (3 M KCl) as the reference electrode and a platinum gauze (99.99%, Sigma-Aldrich) as the counter electrode. The H_2SO_4 catholyte and anolyte (>95%, ACS reagent, Sigma-Aldrich), with concentrations varied from 0.01 M to 0.2 M, were circulated in the flow cell at a constant flow rate of 10 ml min^{-1}. The catholyte and anolyte were separated by a proton exchange membrane (Nafion 117). The CO_2 was supplied at a flow rate of 50 standard cubic centimetres per minute (sccm) by using a digital mass flow controller. All the electrochemical tests were performed though a potentiostat (Autolab PGSTAT302N). The volumes of catholyte and anolyte used for circulation were 25 ml, and the liquid products were collected after 1 h of continuous operation for analysis. Linear sweeping voltammetry measurements were carried out in the same flow cell at a scan rate of 50 mV s^{-1}. All potentials were converted to reversible hydrogen electrode (RHE) via the following equation:

$$E(\mathrm{RHE}) = E(\mathrm{Ag/AgCl}) + 0.210\ \mathrm{V} + 0.059 \times \mathrm{pH} \quad (1)$$

The ohmic resistance and charge transfer resistance were measured through electrochemical impedance spectroscopy (EIS), and the data points were obtained between 0.01 Hz and 200 kHz.

CO_2R product analysis

The gas products were analysed through gas chromatograph (Perkin Elmer Clarus 590) equipped with a thermal conductivity detector and

flame ionization detector. The gas products were controlled in 1 ml volume from the gas outlet and injected into the gas chromatograph for quantification, and the FE was calculated via the following equation:

$$\text{Faradaic efficiency}\ (\%) = \frac{zFP}{RT} \times \upsilon \times \frac{1}{I} \times 100\% \quad (2)$$

where z represents the number of electrons required to produce the product, F represents the Faraday constant, P represents the atmosphere pressure, R represents the ideal gas constant, T represents the temperature, υ represents the gas flow rate of the gas and I represents the total current.

The liquid products were analysed using proton nuclear magnetic resonance spectroscopy (600 MHz Agilent DD2 NMR Spectrometer) under water suppression mode. Dimethyl sulfoxide was used as the reference and deuterium oxide as the lock solvent. The FE of liquid was calculated via the following equation:

$$\text{Faradaic efficiency}\ (\%) = \frac{znF}{It} \times 100\% \quad (3)$$

where z represents the number of electrons required to produce the product, n represents the mole number of products and t represents the electrolysis time.

The SPC of CO_2 was calculated using the following equation[12]:

$$\text{SPC}\ (\%) = \frac{\frac{j}{zF} \times V_m}{\text{Flow rate}} \times 100\% \quad (4)$$

where j represents the partial current density of a specific product and V_m represents the molar volume.

Materials characterization

Scanning electron microscopy cross-section images were obtained in a high-resolution scanning electron microscope (Hitachi S-5200). In situ Raman measurements were obtained using a Renishaw inVia Raman microscope equipped with a water immersion objective (63×) with a 785 nm laser in a modified flow cell. Considering that at current densities greater than 100 mA cm^{-2}, H_2 bubbles generated from Cu will cover the lens and deteriorate the quality of Raman signals, we used 5 mM H_2SO_4 for all the tests and applied a constant current density of 20 mA cm^{-2} for all the in situ measurements. For the potassium-rich cases, 3 M KCl was added in the 5 mM H_2SO_4 electrolyte. CO_2 was supplied to the cathode during all the in situ measurements.

Slim flow cell configuration

The cathodes for the slim flow cell were the CG-medium Cu electrodes with a CG-medium ionomer loading of 3 mg cm^{-2}. The anodes were made by IrO_2-coated Ti felt (0.3 mm thickness) with a loading of 1 mg cm^{-2} (refs. 46,47). The measurements were performed in a slim flow cell with an active area of 1 cm^{-2} accessed with a serpentine channel. The catholyte was circulated in a flow field with a thickness of 0.4 mm as shown in Supplementary Fig. 42. CO_2 was fed into the cathode at a flow rate of 50 sccm by using an accurate mass flow controller. The 0.2 M H_2SO_4 catholyte and anolyte were circulated at a constant flow rate of 5 ml min^{-1} using peristaltic pumps. A cation exchange membrane (Nafion 117, Fuel Cell Store) was used for ion exchange and separation of the cathode and anode.

Multiphysics simulations

The simulation of space charge density and electric field in 1D domain (Supplementary Fig. 5) were performed in the COMSOL Multiphysics package based on the finite-element-method solver (https://www.comsol.com/). The electric double layer at the electrode–electrolyte interface was modelled using the Gouy–Chapman–Stern model[48], which consists of the Stern layer and the diffuse layer. The Stern layer consists of a monolayer of surface-adsorbed hydrated cations on the electrode surface, with a thickness of d_s depending on the hydrated cation. The diffuse layer contains free anions and cations distributed according to the Poisson and Boltzmann law, which forms the concentration gradient away from the electrode surface.

MD simulation

Classical MD simulations of full cells of the Cu/KCl/CG/CO_2 solution interface were performed using LAMMPS[49]. The initial structures of interfaces were constructed using PACKMOL (Supplementary Fig. 9)[50]. Each electrode is composed of four copper (111) layers with a surface area of 51.12 × 48.70 $Å^2$ (3,520 Cu atoms in total). The left and right electrodes are separated by a vacuum region of ~12.5 Å, and the total cell length (z coordinate) is 70.26 Å. The electrolyte initially consists of ~3,600 H_2O molecules and 40 randomly distributed CO_2 molecules (Supplementary Fig. 9a). For Cu/KCl solution, 65 KCl ion pairs (corresponding to a 1 M concentration) were added (Supplementary Fig. 9b). For Cu/CG solution, a $C_{50}H_{51}N_4$ molecule with +1 charge is used as the building block for the ionomer (Supplementary Fig. 9c). The initial structure of $C_{50}H_{51}N_4$ molecule was optimized by Gaussian 16 (ref. 51) B3LYP/6-311 G(d, p) (ref. 52). Considering the size of our model, eight $C_{50}H_{51}N_4$ molecules are added into the solution to model Cu/CG solution and same number of Cl^- ions are added to balance the charge.

The pairwise interactions between atoms were described using Lennard–Jones potential, and the long-range Coulomb interactions were calculated using the particle–particle particle–mesh method with an accuracy of 10^{-5} with a cut-off distance of 12 Å. The SPC/E water model was used to reproduce the aqueous environment, with the SHAKE algorithm to constrain the stretching mode of water. The 12–6 Lennard–Jones potential parameters of Cu were obtained from ref. 53, for KCl from ref. 54 and for CO_2 from ref. 55. Parameters for the ionomer were generated with the Moltemplate[56] using the second generation of general Amber force field (GAFF2) (ref. 57), partial charges were set to fit the electrostatic potential generated with B3LYP/6-31G** by RESP[58] using Gaussian 16 (ref. 51) (Fig. 1b–d). The parameters for the cross atoms were obtained using the Lorentz–Berthelot mixing rules.

The simulations were first performed in NPT ensemble in the 2D-PBC model at 298.15 K and 1 bar. The time step was set to 1 fs and atom positions were updated with Verlet algorithm. The interface was equilibrated by at least 10 ns. The equilibrated interface model was then transferred to a 3D-PBC set-up, in which the electrode potentials can be adjusted using the finite field method implemented in the USER-CONP2 package[59]. The package, described in ref. 59, has been used in simulating electric double layers[60–62]. With this package, we adjusted electrode potentials using the finite field method at fixed potential differences (ΔU) of 0.0, 0.5, 1.0, 1.5, 2.0 and 2.5 V between two electrodes.

The simulations were performed in NVE ensemble at 298.15 K for at least 30 ns. The temperature is adjusted with a canonical sampling thermostat that uses global velocity rescaling with Hamiltonian dynamics[63]. The final 10 ns trajectories were used for post-analysis with MDAnalysis Python package[64] and visualized by OVITO[65].

Data availability

Source data for the stability test shown in Fig. 4a,b and the atomic coordinates of the optimized computational models can be found in figshare[26]. Data that support the findings of this study can be found in the article and Supplementary information. All other data supporting this work are available from the corresponding authors upon reasonable request.

References

1. Li, L., Li, X., Sun, Y. & Xie, Y. Rational design of electrocatalytic carbon dioxide reduction for a zero-carbon network. *Chem. Soc. Rev.* **51**, 1234–1252 (2022).

2. Kibria Nabil, S., McCoy, S. & Kibria, M. G. Comparative life cycle assessment of electrochemical upgrading of CO_2 to fuels and feedstocks. *Green Chem.* **23**, 867–880 (2021).
3. Artz, J. et al. Sustainable conversion of carbon dioxide: an integrated review of catalysis and life cycle assessment. *Chem. Rev.* **118**, 434–504 (2018).
4. Pelayo García de Arquer, F. et al. CO_2 electrolysis to multi-carbon products at activities greater than 1 A cm^{-2}. *Science* **367**, 661–666 (2020).
5. Gabardo, C. M. et al. Continuous carbon dioxide electroreduction to concentrated multi-carbon products using a membrane electrode assembly. *Joule* **3**, 2777–2791 (2019).
6. Wang, Y. et al. Catalyst synthesis under CO_2 electroreduction favours faceting and promotes renewable fuels electrosynthesis. *Nat. Catal.* **3**, 98–106 (2019).
7. Xu, H. et al. Highly selective electrocatalytic CO_2 reduction to ethanol by metallic clusters dynamically formed from atomically dispersed copper. *Nat. Energy* **5**, 623–632 (2020).
8. Ma, M. et al. Insights into the carbon balance for CO_2 electroreduction on Cu using gas diffusion electrode reactor designs. *Energy Environ. Sci.* **13**, 977–985 (2020).
9. Larrazabal, G. O. et al. Analysis of mass flows and membrane cross-over in CO_2 reduction at high current densities in an MEA-type electrolyzer. *ACS Appl. Mater. Interfaces* **11**, 41281–41288 (2019).
10. Ozden, A. et al. Cascade CO_2 electroreduction enables efficient carbonate-free production of ethylene. *Joule* **5**, 706–719 (2021).
11. Blommaert, M. A., Subramanian, S., Yang, K., Smith, W. A. & Vermaas, D. A. High indirect energy consumption in AEM-based CO_2 electrolyzers demonstrates the potential of bipolar membranes. *ACS Appl. Mater. Interfaces* **14**, 557–563 (2022).
12. Huang, J. E. et al. CO_2 electrolysis to multi-carbon products in strong acid. *Science* **372**, 1074–1078 (2021).
13. Gu, J. et al. Modulating electric field distribution by alkali cations for CO_2 electroreduction in strongly acidic medium. *Nat. Catal.* **5**, 268–276 (2022).
14. Xie, Y. et al. High carbon utilization in CO_2 reduction to multi-carbon products in acidic media. *Nat. Catal.* **5**, 564–570 (2022).
15. Monteiro, M. C. O. et al. Absence of CO_2 electroreduction on copper, gold and silver electrodes without metal cations in solution. *Nat. Catal.* **4**, 654–662 (2021).
16. Monteiro, M. C. O., Dattila, F., Lopez, N. & Koper, M. T. M. The role of cation acidity on the competition between hydrogen evolution and CO_2 reduction on gold electrodes. *J. Am. Chem. Soc.* **144**, 1589–1602 (2021).
17. Xu, Y. et al. Self-cleaning CO_2 reduction systems: unsteady electrochemical forcing enables stability. *ACS Energy Lett.* **6**, 809–815 (2021).
18. Endrődi, B. et al. Operando cathode activation with alkali metal cations for high current density operation of water-fed zero-gap carbon dioxide electrolysers. *Nat. Energy* **6**, 439–448 (2021).
19. Ren, W., Xu, A., Chan, K. & Hu, X. A cation concentration gradient approach to tune the selectivity and activity of CO_2 electroreduction. *Angew. Chem. Int. Ed.* **61**, e2022141 (2022).
20. Ma, Z. et al. CO_2 electroreduction to multi-carbon products in strongly acidic electrolyte via synergistically modulating the local microenvironment. *Nat. Commun.* **13**, 7596 (2022).
21. Resasco, J. et al. Promoter effects of alkali metal cations on the electrochemical reduction of carbon dioxide. *J. Am. Chem. Soc.* **139**, 11277–11287 (2017).
22. Ummireddi, A. K., Sharma, S. K. & Pala, R. G. S. Ammonium ionic liquid cation promotes electrochemical CO_2 reduction to ethylene over formate while inhibiting the hydrogen evolution on a copper electrode. *Catal. Sci. Technol.* **12**, 519–529 (2022).
23. Pankhurst, J. R., Guntern, Y. T., Mensi, M. & Buonsanti, R. Molecular tunability of surface-functionalized metal nanocrystals for selective electrochemical CO_2 reduction. *Chem. Sci.* **10**, 10356–10365 (2019).
24. Zhong, S. et al. Efficient electrochemical transformation of CO_2 to C_2/C_3 chemicals on benzimidazole-functionalized copper surfaces. *Chem. Commun.* **54**, 11324–11327 (2018).
25. Banerjee, S., Gerke, C. S. & Thoi, V. S. Guiding CO_2RR selectivity by compositional tuning in the electrochemical double layer. *Acc. Chem. Res.* **55**, 504–515 (2022).
26. Fan, M. et al. Cationic-group functionalized electrocatalysts enable stable acidic CO_2 electrolysis. *figshare* https://doi.org/10.6084/m9.figshare.22819415 (2023).
27. Wright, A. G. et al. Hexamethyl-*p*-terphenyl poly(benzimidazolium): a universal hydroxide-conducting polymer for energy conversion devices. *Energy Environ. Sci.* **9**, 2130–2142 (2016).
28. Fan, J. et al. Poly(bis-arylimidazoliums) possessing high hydroxide ion exchange capacity and high alkaline stability. *Nat. Commun.* **10**, 2306 (2019).
29. Fan, J. et al. Cationic polyelectrolytes, stable in 10 M KOH_{aq} at 100 °C. *ACS Macro Lett.* **6**, 1089–1093 (2017).
30. Ge, A. et al. Interfacial structure and electric field probed by in situ electrochemical vibrational Stark effect spectroscopy and computational modeling. *J. Phys. Chem. C* **121**, 18674–18682 (2017).
31. Chen, L. D., Urushihara, M., Chan, K. & Nørskov, J. K. Electric field effects in electrochemical CO_2 reduction. *ACS Catal.* **6**, 7133–7139 (2016).
32. Harroun, S. G. et al. Electrochemical surface-enhanced Raman spectroscopy (E-SERS) of novel biodegradable ionic liquids. *Phys. Chem. Chem. Phys.* **15**, 19205–19212 (2013).
33. Fu, J. Y. et al. In situ Raman monitoring of potential-dependent adlayer structures on the Au(111)/ionic liquid interface. *Langmuir* **38**, 6209–6216 (2022).
34. Dunwell, M., Yan, Y. & Xu, B. Understanding the influence of the electrochemical double-layer on heterogeneous electrochemical reactions. *Curr. Opin. Chem. Eng.* **20**, 151–158 (2018).
35. Malkani, A. S. et al. Understanding the electric and non-electric field components of the cation effect on the electrochemical CO reduction reaction. *Sci. Adv.* **6**, eabd2569 (2020).
36. Salvatore, D. A. et al. Designing anion-exchange membranes for CO_2 electrolysers. *Nat. Energy* **6**, 339–348 (2021).
37. Deimede, V., Voyiatzis, G. A., Kallitsis, J. K., Qingfeng, L. & Bjerrum, N. J. Miscibility behavior of polybenzimidazole/sulfonated polysulfone blends for use in fuel cell applications. *Macromolecules* **33**, 7609–7617 (2000).
38. Li, Q., He, R., Berg, R. W., Hjuler, H. A. & Bjerrum, N. J. Water uptake and acid doping of polybenzimidazoles as electrolyte membranes for fuel cells. *Solid State Ion.* **168**, 177–185 (2004).
39. Quartarone, E. et al. Pyridine-based PBI composite membranes for PEMFCs. *Fuel Cells* **9**, 349–355 (2009).
40. Chen, Z. Water balancing. *Nat. Energy* **5**, 12–13 (2020).
41. Bonn, M. et al. Suppression of proton mobility by hydrophobic hydration. *J. Am. Chem. Soc.* **131**, 17070–17071 (2009).
42. Zhang, C. et al. Water at hydrophobic interfaces delays proton surface-to-bulk transfer and provides a pathway for lateral proton diffusion. *Proc. Natl Acad. Sci. USA* **109**, 9744–9749 (2012).
43. Liu, X. et al. pH effects on the electrochemical reduction of $CO_{(2)}$ towards C_2 products on stepped copper. *Nat. Commun.* **10**, 32 (2019).
44. Cao-Thang, D. et al. CO_2 electroreduction to ethylene via hydroxide-mediated copper catalysis at an abrupt interface. *Science* **360**, 783–787 (2018).

45. Hori, Y. et al. 'Deactivation of copper electrode' in electrochemical reduction of CO_2. *Electrochim. Acta* **50**, 5354–5369 (2005).
46. Miao, R. K. et al. Electroosmotic flow steers neutral products and enables concentrated ethanol electroproduction from CO_2. *Joule* **5**, 2742–2753 (2021).
47. O'Brien, C. P. et al. Single pass CO_2 conversion exceeding 85% in the electrosynthesis of multi-carbon products via local CO_2 regeneration. *ACS Energy Lett.* **6**, 2952–2959 (2021).
48. Stern, O. Zur Theorie der elektrolytischen Doppelschicht. *Z. Elektrochem. Angew. Physikal. Chem.* **30**, 508–516 (1924).
49. Thompson, A. P. et al. LAMMPS—a flexible simulation tool for particle-based materials modeling at the atomic, meso, and continuum scales. *Comput. Phys. Commun.* **271**, 108171 (2022).
50. Martinez, L., Andrade, R., Birgin, E. G. & Martinez, J. M. PACKMOL: a package for building initial configurations for molecular dynamics simulations. *J. Comput. Chem.* **30**, 2157–2164 (2009).
51. Gaussian 16 Rev. C.01 (Gaussian, 2016).
52. Krishnan, R., Binkley, J. S., Seeger, R. & Pople, J. A. Self-consistent molecular orbital methods. XX. A basis set for correlated wave functions. *J. Chem. Phys.* **72**, 650–654 (1980).
53. Heinz, H., Vaia, R. A., Farmer, B. L. & Naik, R. R. Accurate simulation of surfaces and interfaces of face-centered cubic metals using 12–6 and 9–6 Lennard–Jones potentials. *J. Phys. Chem. C* **112**, 17281–17290 (2008).
54. Joung, I. S. & Cheatham, T. E. III. Determination of alkali and halide monovalent ion parameters for use in explicitly solvated biomolecular simulations. *J. Phys. Chem. B* **112**, 9020–9041 (2008).
55. Sun, C., Wen, B. & Bai, B. Application of nanoporous graphene membranes in natural gas processing: molecular simulations of CH_4/CO_2, CH_4/H_2S and CH_4/N_2 separation. *Chem. Eng. Sci.* **138**, 616–621 (2015).
56. Jewett, A. I. et al. Moltemplate: a tool for coarse-grained modeling of complex biological matter and soft condensed matter physics. *J. Mol. Biol.* **433**, 166841 (2021).
57. He, X., Man, V. H., Yang, W., Lee, T.-S. & Wang, J. A fast and high-quality charge model for the next generation general AMBER force field. *J. Chem. Phys.* **153**, 114502 (2020).
58. Bayly, C. I., Cieplak, P., Cornell, W. & Kollman, P. A. A well-behaved electrostatic potential-based method using charge restraints for deriving atomic charges: the RESP model. *J. Phys. Chem.* **97**, 10269–10280 (1993).
59. Tee, S. R. & Searles, D. J. Fully periodic, computationally efficient constant potential molecular dynamics simulations of ionic liquid supercapacitors. *J. Chem. Phys.* **156**, 184101 (2022).
60. Ahrens-Iwers, L. J. V., Janssen, M., Tee, S. R. & Meissner, R. H. ELECTRODE: an electrochemistry package for atomistic simulations. *J. Chem. Phys.* **157**, 084801 (2022).
61. Langford, L. et al. Constant-potential molecular dynamics simulations of molten-salt double layers for FLiBe and FLiNaK. *J. Chem. Phys.* **157**, 094705 (2022).
62. Li, X. Y. et al. Molecular understanding of the Helmholtz capacitance difference between Cu(100) and graphene electrodes. *J. Chem. Phys.* **158**, 084701 (2023).
63. Bussi, G., Donadio, D. & Parrinello, M. Canonical sampling through velocity rescaling. *J. Chem. Phys.* **126**, 014101 (2007).
64. Michaud-Agrawal, N., Denning, E. J., Woolf, T. B. & Beckstein, O. MDAnalysis: a toolkit for the analysis of molecular dynamics simulations. *J. Comput. Chem.* **32**, 2319–2327 (2011).
65. Stukowski, A. Visualization and analysis of atomistic simulation data with OVITO—the Open Visualization Tool. *Model. Simul. Mat. Sci. Eng.* **18**, 015012 (2010).

Acknowledgements

We acknowledge support from the Natural Sciences and Engineering Research Council (NSERC) of Canada and TotalEnergies SE. Support from Canada Research Chairs Program is also gratefully acknowledged. Infrastructure provided through the Canada Foundation for Innovation and the Ontario Research Fund supported the work. R.K.M. thanks NSERC, Hatch and the Government of Ontario for their support through graduate scholarships. P.O. thanks the Climate Positive Energy for its support through Rising Stars in Clean Energy Postdoctoral Fellowship. Density functional theory calculations were performed on the Niagara supercomputer at the SciNet HPC Consortium. SciNet is funded by: the Canada Foundation for Innovation; the Government of Ontario; Ontario Research Fund - Research Excellence; and the University of Toronto. The computational study is supported by the Marsden Fund Council from Government funding (21-UOA-237) and Catalyst: Seeding General Grant (22-UOA-031-CGS), managed by Royal Society Te Apārangi. Z.W. and Y.M. acknowledge the use of New Zealand eScience Infrastructure (NeSI) high-performance computing facilities, consulting support and/or training services as part of this research. G.I.N.W. and Y.M. acknowledge funding support from the MacDiarmid Institute for Advanced Materials and Nanotechnology, the Energy Education Trust of New Zealand and the Royal Society Te Apārangi. Z.W. and Y.M. graciously acknowledge D. J. Searles (University of Queensland) and J. Cheng (Xiamen University) for their support and scientific discussions on the computational work.

Author contributions

D.S. and E.H.S. supervised the project. M.F., J.E.H. and R.K.M. designed and carried out all the experiments. J.E.H. conceived the idea. Y.M., P.O. and Y.C. carried out the MD simulation. Z.W. supervised the MD simulation. Y.M., Y.C., G.I.N.W. and Z.W. analysed the MD simulation results. M.F. and J.E.H. analysed the experimental data and prepared the paper. R.K.M. performed the slim-flow cell design and experiments. F.L. carried out the COMSOL simulation. M.F. carried out all EIS measurements and analysed data. J.E.H. and Z.C. carried out the SERS measurements, and M.F. analysed the SERS data. Z.Z. performed the pH-sensitive Raman tests. J.Z., A.O. and Y.W. synthesized catalysts. W.N. and Y.Z. carried out scanning electron microscopy characterization. Y.Y. performed the X-ray diffraction characterization. B.K. and K.G. carried out the contact angle measurements. C.P.O., Y.X. and Y.C.X. performed product analysis. All authors discussed the results and assisted during paper preparation.

Competing interests

There is a US provisional patent application (63/381.180) titled 'A modified catalyst for operating electrochemical carbon dioxide reduction in a non-alkali acidic medium and related techniques', filed by the authors M.F., J.E.H., R.K.M., E.H.S. and D.S of this article and their institutions. The other authors declare no competing interests.

Additional information

Supplementary information The online version contains supplementary material available at https://doi.org/10.1038/s41929-023-01003-5.

Correspondence and requests for materials should be addressed to Ziyun Wang, Edward H. Sargent or David Sinton.

Peer review information *Nature Catalysis* thanks Peng Kang and the other, anonymous, reviewer(s) for their contribution to the peer review of this work.